Frequency stabilisation of a laser at 674 nm for coherent manipulation of $^{88}Sr^{+}$ ions

Erik Jansson

Master Thesis in Physics,
Stockholm University
April 28, 2020

Supervisor: Markus Hennrich
Assistant supervisor: Gerard Higgins

Fysikum/ Department of Physics
Examensarbete 60 hp /Degree 60 HE credits
Fysik/ Physics
Masterprogrammet i fysik (120 hp) / Master in Physics (120 credits)
Höstterminen 2018 – Vårterminen 2020 /
Autumn term 2018 - Spring term 2020

Abstract

A stable qubit laser is essential in order to perform high fidelity qubit operations on trapped ions. In this thesis an experimental setup for a new qubit laser at 674 nm is built and the laser frequency is stabilised by locking it to a high finesse cavity using the Pound-Drever-Hall technique. An upper limit of the qubit laser linewidth of (123 ± 6) Hz was obtained by a heterodyne beat note measurement between the new qubit laser and the old one. The laser and high finesse cavity were further characterised and experiments on an ion were conducted using the new laser. The ion had a coherence time of $\tau = (1050 \pm 90)\mu$s, when it was probed using the new laser by driving Rabi oscillations between electronic states of the $^{88}Sr^{+}$ ion.

Contents

Chapter 1

Introduction

In the past 50 years quantum computers have been developed from an initial idea to the realisation of small quantum processors. One of the most successful experimental platforms for implementing a prototype quantum computer is a system of trapped atomic ions. The idea of using trapped ions for quantum computation was proposed in 1995 by Cirac and Zoller [1] who developed a scheme for realizing a two-qubit gate with ions by exchanging quantum information via their common motion in a trapping potential. Since then, trapped ions has become one of the leading platforms in the race toward realizing a quantum computer, a machine that is more powerful than a classical computer. In 2000 DiVincenzo [2] outlined certain conditions which must be fulfilled for building a quantum computer. They are

1. A scalable system with well characterized qubits.
2. Ability to initialize qubits in a state that can be reliably reproduced.
3. Decoherence times much longer than the gate operation time.
4. A "universal" set of quantum gates.
5. A qubit-specific measurement capability.

DiVincenzo also outlined two additional criteria necessary for quantum networks, but since this thesis focuses on the laser manipulation of qubit states and not on quantum networks they do not concern us here. For trapped ions, the last 4 criteria are fulfilled by using the ions internal electronic states for storing qubits and coupling several qubits via their common vibrational modes. However, when increasing the number of ions, the number of motional modes also increases and the mode spectrum of the system becomes more crowded. Therefore, the control of the coupling to vibrational modes becomes increasingly difficult and the gate operations slow down. This limits the potential for scalability. In 2008, Müller et al.[3] proposed using the dipole-dipole interaction between highly-excited Rydberg ions to conduct a two-qubit gate instead of using the vibrational modes of ordinary ions. This coupling mechanism does not

slow down for more ions and thus has potential to avoid the scalability problem. The ion trapping experiment at Stockholm University was built to perform quantum computation via Rydberg interaction. The qubits are encoded in low-lying electronic states and for coupling qubits the ions are excited to Rydberg states [4]. This thesis focuses on manipulating the quantum states of qubits in low-lying electronic states. It involves setting up an improved new laser system for addressing the transition between qubit states, as well as characterising the new laser. This laser features an intra-cavity electro-optic modulator (EOM) which increases the feedback bandwidth for laser stabilisation. The EOM shifts the servo-bumps of the stabilisation to larger frequencies and reduces their amplitude. This results in a cleaner spectrum of the laser and thus gives a more precise qubit manipulation.

Chapter 2

Theoretical background

This chapter outlines the theoretical background of the thesis. The first section (section 2.1) describes how trapped strontium $^{88}Sr^{+}$ ions can be used in quantum computation and measurements for determining some limitations of the system. The second section (section 2.2) focuses on optical cavities and laser stabilisation. It describes an experimental technique for stabilising a laser using an optical cavity. The third section (section 2.3) describes the control system used to control different parameters related to the stabilisation of the laser such as temperature.

2.1 Ions

2.1.1 Trapped ions as qubits

In classical computers, the smallest unit for storing information is a bit whose states are usually represented as 0 and 1. In quantum computers the smallest unit for storing information is a quantum bit or qubit. A qubit is stored in a quantum system which has two well-defined states labelled $|0\rangle$ and $|1\rangle$, they provide the basis for the qubit [5]. The qubit can be in state $|0\rangle$, state $|1\rangle$ or in a superposition state of the two

$$|\psi\rangle = c_0 |0\rangle + c_1 |1\rangle \tag{2.1}$$

where c_0 and c_1 are complex numbers that obey the normalisation condition $|c_0|^2 + |c_1|^2 = 1$.

In the experimental setup presented in this thesis the qubits are encoded in electronic states of a strontium $^{88}Sr^{+}$ ion trapped in a linear Paul trap. The qubit state $|0\rangle$ corresponds to a Zeeman sublevel of the $4D_{5/2}$ metastable state of the ion and the state $|1\rangle$ corresponds to a Zeeman sublevel of the $5S_{1/2}$ ground state. Simple qubit quantum gate operations are implemented using laser pulses at 674 nm that drive the qubit transition $5S_{1/2} \leftrightarrow 4D_{5/2}$ (See figure 2.2 for more details).

2.1.2 The ion trap

The linear Paul trap operates with a combination of static and oscillating electric quadrupole fields that dynamically confine a string of ions [4]. Figure 2.1 shows the trap setup. The voltages applied to the blade electrodes generate the oscillating electric quadrupole field confining the ions in a two-dimensional radial quadrupole potential

$$\Phi(x, y, z) = \frac{U_{\mathrm{rf}}}{2r_0^2} \cos(\Omega_{\mathrm{rf}} t)(x^2 - y^2) \tag{2.2}$$

where U_{rf} is the rf-potential difference between opposing electrodes, r_0 is the minimum distance between the trapping axis and the electrodes and Ω_{rf} is the frequency of the rf-potential, in the experiment typically $\Omega_{\mathrm{rf}} \approx 2\pi \times 18.2$ MHz. The voltages applied to the endcap electrodes generate the static electric field that traps the ions along the z-axis. Positive voltages are applied to the endcaps so that the positive ions are repelled by the endcaps and thus trapped in the z-direction. The oscillating field together with the static field traps the ions in all three dimensions. The motion of the ions in the radial directions (x and y) consists of two parts: the harmonic motion with frequencies ω_x, ω_y called the secular motion and the faster driven motion of frequency Ω_{rf} called micromotion. In the axial (z) direction there is no oscillating field and therefore the motion is just the secular motion with frequency ω_z. (For more details on the trap setup see the master thesis of Fabian Pokorny [6] and the PhD-thesis by Gerard Higgins [4]).

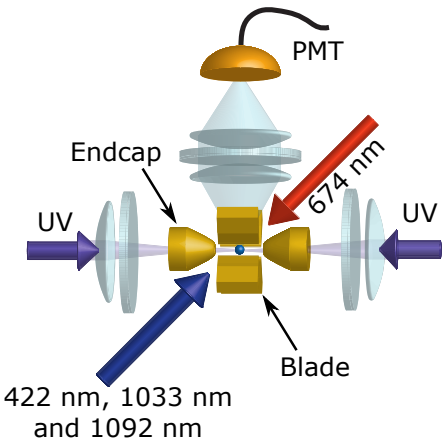

Figure 2.1: The ion trap setup with the laser directions, the photomultiplier tube (PMT), endcap electrodes and blade electrodes.

2.1.3 The Zeeman effect and laser transitions

For atomic levels in the LS-coupling regime with quantum numbers L, S and J, there are $(2J + 1)$ degenerate m_J-states. By applying a magnetic field this

degeneracy can be lifted resulting in the splitting of the atomic levels into magnetic sub-levels. This effect is called the Zeeman effect and the splitting of the sub-levels is referred to as the Zeeman splitting [5]. The energy of an atom in a magnetic field **B** applied along the z-axis is then

$$\Delta E = -\boldsymbol{\mu} \cdot \mathbf{B} = -\mu_z B_z \tag{2.3}$$

where $\boldsymbol{\mu}$ is the magnetic dipole moment of the atom and μ_z is its z-component given by

$$\mu_z = -g\mu_B m_J \tag{2.4}$$

with μ_B the Bohr magneton and the g-factor which can be well approximated by the Landé g-factor g_J

$$g_J = 1 + \frac{J(J+1) + S(S+1) - L(L+1)}{2J(J+1)}. \tag{2.5}$$

Finally, the energy becomes

$$\Delta E = g_J \mu_B B_z m_J \tag{2.6}$$

Figure 2.2 shows an energy level scheme for $^{88}Sr^+$ with the Zeeman splitting of the levels with the magnetic quantum numbers m_J as well as the qubit states.

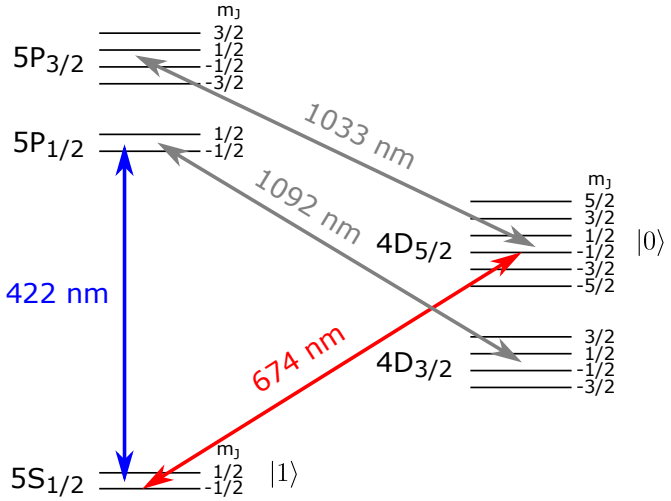

Figure 2.2: The energy level scheme for $^{88}Sr^+$ with the Zeeman splitting of the levels. The wavelengths correspond to the laser fields which drive the respective transitions.

The laser transitions in figure 2.2 are important for qubit operations. The sub-levels that are used for state $|1\rangle$ and state $|0\rangle$ depends on what the qubit is going to be used for. An example of a transition used in this thesis is the $5S_{1/2}(m_J = -1/2) \leftrightarrow 4D_{5/2}(m_J = -5/2)$ transition, but any allowed transition could in principle be used. The qubit state is manipulated using the 674 nm

laser which is called the qubit laser. The 422 nm laser is used for state detection. Since the natural decay rate of the $5P_{1/2}$ state is $2\pi \times 22$MHz, there are a lot of photons scattered in a short time interval when the transition $5S_{1/2} \leftrightarrow 5P_{1/2}$ is driven strongly by the 422 nm laser. These photons can be detected using a camera or a photomultiplier tube. The 422 nm laser is also employed for Doppler cooling. The 1092 nm laser pumps the ion from $4D_{3/2}$ back to $5S_{1/2}$ closing the cooling-detection cycle. It counteracts optical pumping to the $4D_{3/2}$ state due to the decay from $5P_{1/2}$ to the $4D_{3/2}$ state. The 1033 nm laser is used for initialising the system, it removes population from the $4D_{5/2}$ state. It is also used for shortening the effective $4D_{5/2}$ lifetime during resolved sideband cooling [4].

2.1.4 Ion and laser interaction

An electromagnetic field on resonance to a two-level quantum system can drive the quantum system and leads to a cyclic behaviour. As it evolves in time the state of the system will oscillate between the two levels at a frequency called the Rabi frequency (section 3.2.3 shows the experimental data of Rabi oscillations). Over time the amplitude of the oscillations will decrease due to the loss of coherence between the driving field and the two-level system. Therefore the decay time of the amplitude of the Rabi oscillations also known as the coherence time will give an indication of how long the system and the laser field stay coherent.

In a trapped ion experiment the trapping potential of the Paul trap can be described as a harmonic pseudo-potential and therefore the Hamiltonian of a trapped ion will contain a harmonic term. The total Hamiltonian of a two-level system with electronic ground state $|g\rangle$ and excited state $|e\rangle$ can be described as a sum of three Hamiltonians, the Hamiltonian of the electronic states of the ion $\hat{H}_{\mathrm{e}}$, the quantum harmonic term $\hat{H}_{\mathrm{m}}$ of the ion motion and the Hamiltonian of the interaction $\hat{H}_{\mathrm{int}}$ between laser field and ion. Following the discussion in the Master thesis by N. Röck [7]

$$\hat{H} = \hat{H}_{\mathrm{e}} + \hat{H}_{\mathrm{m}} + \hat{H}_{\mathrm{int}}. \tag{2.7}$$

The Hamiltonian of a two-level system is

$$\hat{H}_{\mathrm{e}} = \frac{1}{2}\hbar\omega_{eg}\hat{\sigma}_z \tag{2.8}$$

where ω_{eg} is the laser frequency resonant to the transition $|g\rangle \leftrightarrow |e\rangle$ and $\hat{\sigma}_z$ is the Pauli matrix. For a single motional mode the Hamiltonian is

$$\hat{H}_{\mathrm{m}} = \hbar\omega\left(\hat{a}^\dagger\hat{a} + \frac{1}{2}\right) = \hbar\omega\left(\hat{n} + \frac{1}{2}\right) \tag{2.9}$$

where $\hat{n}$ is the number operator and ω is the secular motional frequency. In the experiment described in this thesis the secular motional frequency is the motional frequency of the ions in the radial direction of the trap described in

section 2.1.2. Finally, the interaction between the two-level system and the electromagnetic field is described by

$$\hat{H}_{\text{int}} = \frac{1}{2}\hbar\Omega\left(\hat{\sigma}^{+} + \hat{\sigma}^{-}\right)\left(e^{i(\omega_l t - k_l \hat{r})} + e^{-i(\omega_l t - k_l \hat{r})}\right) \tag{2.10}$$

where ω_l and k_l is the frequency and wave number of the laser light, $\hat{\sigma}^{+}$ and $\hat{\sigma}^{-}$ are Pauli raising and lowering operators, Ω is the Rabi-frequency of the transition and $\hat{r}$ is the ion position operator. If $\hat{r}$ is in the direction of the ion motion it can be described as

$$\hat{r} = \sqrt{\frac{\hbar}{2m\omega}}\left(\hat{a}^{\dagger} + \hat{a}\right) \tag{2.11}$$

The Lamb-Dicke parameter η is defined as

$$\eta = k_l\sqrt{\frac{\hbar}{2m\omega}} \tag{2.12}$$

Therefore the Hamiltonian of the interaction between laser and ion can be described as

$$\hat{H}_{\text{int}} = \frac{1}{2}\hbar\Omega\left(\hat{\sigma}^{+} + \hat{\sigma}^{-}\right)\left(e^{i\left[\omega_l t - \eta\left(\hat{a}^{\dagger} + \hat{a}\right)\right]} + e^{-i\left[\omega_l t - \eta\left(\hat{a}^{\dagger} + \hat{a}\right)\right]}\right) \tag{2.13}$$

To simplify $\hat{H}_{\text{int}}$ the unitary transform $\hat{U} = e^{i(\hat{H}_{\text{e}} + \hat{H}_{\text{m}})t/\hbar}$ is used to move from the Schrödinger picture to the interaction picture where the interaction Hamiltonian is $\hat{H}_{\text{I}} = \hat{U}^{\dagger}\hat{H}_{\text{int}}\hat{U}$. This leads to $e^{\pm i(\omega_l \pm \omega_{eg})}$ terms. In the rotating wave approximation the $\omega_l + \omega_{eg}$ term is neglected since it oscillates fast and is not energy conserving. Thus, only the $\omega_l - \omega_{eg} \ll \omega_{eg}$ term is left. The interaction Hamiltonian becomes

$$\hat{H}_{\text{I}} = \frac{1}{2}\hbar\Omega\left(\hat{\sigma}^{+}e^{-i\Delta t}e^{\left[i\eta\left(\hat{a}e^{-i\omega t} + \hat{a}^{\dagger}e^{i\omega t}\right)\right]} + h.c.\right) \tag{2.14}$$

where $\Delta = \omega_l - \omega_{eg}$ and $h.c.$ is the Hermitian conjugate. Assuming the ion is spatially confined to a region significantly smaller than the wavelength of the laser field, then it is in the so called Lamb-Dicke regime. This regime is defined by the condition

$$\eta^2\left(2n + 1\right) \ll 1 \tag{2.15}$$

where n is the phonon occupation number. In this regime, the second exponential term, in equation (2.14) can be Taylor-expanded to

$$e^{i\eta\left(\hat{a}e^{-i\omega t} + \hat{a}^{\dagger}e^{i\omega t}\right)} = 1 + i\eta\left(\hat{a}e^{-i\omega t} + \hat{a}^{\dagger}e^{i\omega t}\right) - \frac{\eta^2}{2}\left(\hat{a}e^{-i\omega t} + \hat{a}^{\dagger}e^{i\omega t}\right)^2 + \mathcal{O}(\eta^3). \tag{2.16}$$

Considering only the first and second order terms in equation (2.16) and inserting those into equation (2.14), the interaction Hamiltonian becomes

$$\begin{aligned}\hat{H}_I = &\frac{1}{2}\hbar\Omega\left(1-\eta^2\hat{a}^\dagger\hat{a}\right)\left(\hat{\sigma}^+e^{-i\Delta t}+\hat{\sigma}^-e^{i\Delta t}\right)\\ &+i\frac{\hbar\Omega\eta}{2}\left(\hat{a}e^{-i\omega t}+\hat{a}^\dagger e^{i\omega t}\right)\hat{\sigma}^+e^{-i\Delta t}\\ &-i\frac{\hbar\Omega\eta}{2}\left(\hat{a}e^{-i\omega t}+\hat{a}^\dagger e^{i\omega t}\right)\hat{\sigma}^-e^{i\Delta t}\\ &-\frac{\hbar\Omega\eta^2}{4}\left(\hat{a}^2e^{-2i\omega t}+(\hat{a}^\dagger)^2e^{2i\omega t}\right)\left(\hat{\sigma}^+e^{-i\Delta t}+\hat{\sigma}^-e^{i\Delta t}\right)\end{aligned} \tag{2.17}$$

From this expression three important cases can be determined.

- When $\Delta = 0$, the laser frequency is tuned to resonance and the $|g,n\rangle \leftrightarrow |e,n\rangle$ transition is driven as shown in figure 2.5. This is called the carrier transition. Assuming that the coupling strength of the terms that oscillates off-resonantly are much smaller than the detuning and therefore can be neglected, the equation (2.17) can be reduced to

$$\hat{H}_{I_{\text{carrier}}} = \frac{1}{2}\hbar\Omega_{n,n}\left(\hat{\sigma}^+ + \hat{\sigma}^-\right) \qquad \text{with} \qquad \Omega_{n,n} = \Omega\left(1-\eta^2 n\right) \tag{2.18}$$

  where $\Omega_{n,n}$ is the coupling strength and $\langle\hat{a}^\dagger\hat{a}\rangle = n$ is the phonon occupation number as described in the condition for the Lamb-Dicke regime (2.15).

- When $\Delta = -\omega$, the laser frequency is detuned to drive the transition $|g,n\rangle \leftrightarrow |e,n-1\rangle$ (See figure 2.5). This is called the first red sideband. By once again neglecting the terms that oscillates off-resonantly, the equation (2.17) can be reduced to

$$\hat{H}_{I_{\text{red}}} = \frac{1}{2}i\hbar\Omega_{n,n-1}\left(|e,n-1\rangle\langle g,n| - |g,n\rangle\langle e,n-1|\right) \tag{2.19}$$

  with $\Omega_{n,n-1} = \eta\sqrt{n}\Omega$

- When $\Delta = +\omega$, the laser frequency is detuned to drive the transition $|g,n\rangle \leftrightarrow |e,n+1\rangle$ (See figure 2.5). This is called the first blue sideband. By following the same argument as above the equation (2.17) can be reduced to

$$\hat{H}_{I_{\text{blue}}} = \frac{1}{2}i\hbar\Omega_{n,n+1}\left(|e,n+1\rangle\langle g,n| - |g,n\rangle\langle e,n+1|\right) \tag{2.20}$$

  with $\Omega_{n,n+1} = \eta\sqrt{n+1}\Omega$

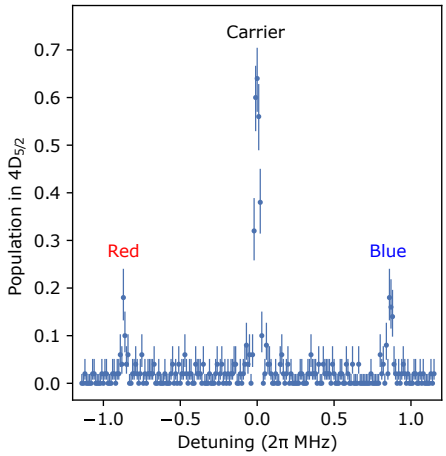

Figure 2.3: A frequency spectrum showing the carrier and sidebands for the qubit transition $5S_{1/2} \leftrightarrow 4D_{5/2}$.

Figure 2.3 shows the frequency spectrum of the qubit transition $5S_{1/2} \leftrightarrow 4D_{5/2}$ with the carrier, the red sideband and the blue sideband. The spectrum was kindly provided by Gerard Higgins.

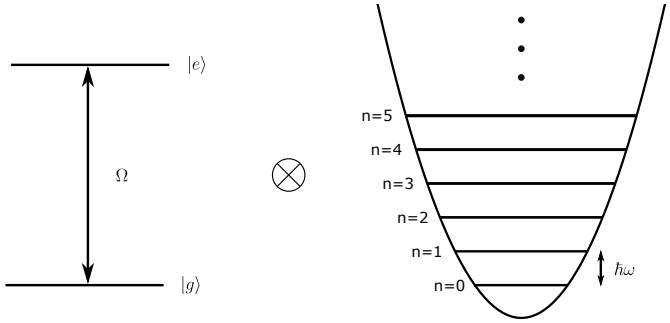

Figure 2.4: The simplified Hilbert space of a trapped ion is represented by a two-level system coupled to a harmonic trapping potential. The combined Hilbert state is spanned by the product states of the two sub-Hilbert spaces.

Figure 2.4 shows a two-level system, in this case the qubit transition $5S_{1/2} \leftrightarrow 4D_{5/2}$, coupled to a harmonic trapping potential. The coupling between and laser field can be illustrated in a "ladder scheme" of the energy levels as depicted in figure 2.5.

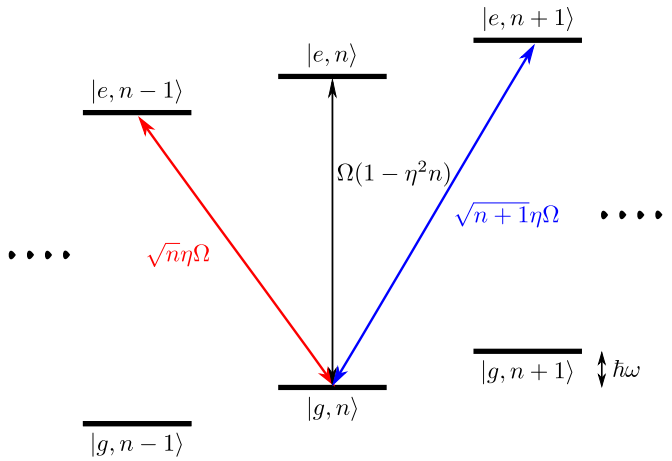

Figure 2.5: A "ladder scheme" for a trapped ion with the carrier transition in black and the red and blue sideband transitions in the respective colours, as well as the coupling strength for each case.

2.1.5 Ramsey experiment

Ramsey pulse sequences are generally used to characterise the coherence time (dephasing time) of a two-level system. A Ramsey-type experiment consists of two resonant $\pi/2$-pulses with some waiting time in between. In the case of a two level system starting from state $|1\rangle$ (See figure 2.6a) the state is driven to a superposition state $(|0\rangle + |1\rangle)/\sqrt{2}$ after the first pulse (See figure 2.6b). During the waiting time the state evolves picking up an extra phase due to e.g. laser frequency or magnetic field fluctuations (See figure 2.6c). Because of the dephasing of the system the final state after the second pulse will not be perfectly $|0\rangle$, but rather some superposition or mixed state, it depends on the accumulated phase (See figure 2.6d). By taking multiple measurements while increasing the waiting time between the pulses the contrast will decay. This decay is related to the coherence time[4]. The decay type will depend on the type of noise that dominates the decoherence process. If the dominant noise is white, the decay will follow an exponential distribution. However if there is temporal correlation in the noise it might follow e.g. a Gaussian distribution. (For more details on the theoretical background of the decay see the master thesis of Anders Lindberg [8]).

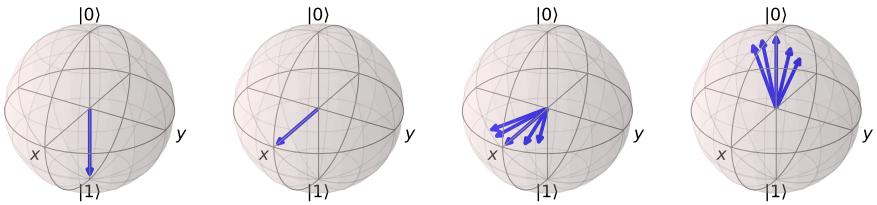

(a) **(b)** **(c)** **(d)**

Figure 2.6: **(a)** The system is in the initial state $|1\rangle$. **(b)** A $\pi/2$-pulse takes the system to a superposition state $(|0\rangle + |1\rangle)/\sqrt{2}$. **(c)** The state evolves randomly during the wait time. **(d)** A second $\pi/2$-pulse takes the evolved state towards state $|0\rangle$, but depending on the evolution of the state in **(c)** the final state will be another superposition state or mixed state.

2.2 Optical cavities and laser stabilisation

In order to manipulate ion qubits a laser with a stable frequency is essential. Laser frequency fluctuations cause dephasing of the laser with respect to the qubit, which limits the time during which the qubit can be manipulated successfully. The stabilisation of the laser frequency can be done by sending the laser light onto a stable reference cavity, e.g. a Fabry-Pérot cavity described in section 2.2.1, and then frequency locking the laser using the Pound-Drever-Hall technique as described in section 2.2.3.

2.2.1 Fabry-Pérot cavity

Consider a Fabry-Pérot cavity in vacuum that consists of two parallel highly reflective mirrors at a distance L from each other. When light enters the cavity it is reflected back and forth inside. Constructive interference will occur when the light entering and the light circulating inside are in phase with each other [9]. Only electromagnetic waves where the optical path of one round trip is an integer multiple q of the wavelength λ will form inside the cavity

$$\lambda q = 2L \tag{2.21}$$

Since the frequency of the light in vacuum is related to the wavelength in the following way

$$\nu = \frac{c}{\lambda} \tag{2.22}$$

the resonances appear periodically at frequency $\nu_q = q\frac{c}{2L}$. The frequency separation of these modes is called the free spectral range ν_{FSR}

$$\nu_{\mathrm{FSR}} = \frac{c}{2L} \tag{2.23}$$

The incident electromagnetic wave E_{in} can be described by

$$E_{\mathrm{in}} = E_0 e^{i(\omega t - kx)} \tag{2.24}$$

where ω is the angular frequency of the light, t the time, k the wavenumber ($k = \frac{2\pi}{\lambda}$) and x the direction of propagation of the wave. For each round-trip of the wave inside the cavity, the wave will pick up a phase

$$\varphi = 2kL = \frac{4\pi L\nu}{c} = \frac{2\pi\nu}{\nu_{\mathrm{FSR}}} \tag{2.25}$$

Each time an electromagnetic wave hits a mirror surface of the cavity, part of the wave will be transmitted with an amplitude t. The other part will be reflected with an amplitude r. For simplicity, in the following discussion it is assumed that the coefficients are the same for both mirrors and that losses can be ignored i.e. $|r|^2 + |t|^2 = 1$ [10].

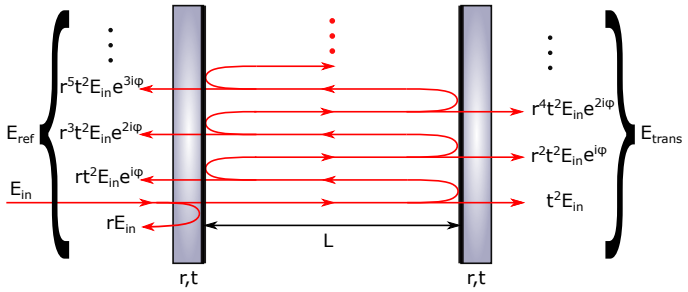

Figure 2.7: A schematic representation of light in a cavity. When light hits a mirror surface, part of the light is transmitted, part is reflected.

Looking at the schematic representation of the light travelling inside the cavity shown in figure 2.7, the sum of the reflected beams E_{ref} is

$$\begin{aligned} E_{\mathrm{ref}} &= -rE_{\mathrm{in}} + rt^2E_{\mathrm{in}}e^{i\varphi} + r^3t^2E_{\mathrm{in}}e^{i2\varphi} + r^5t^2E_{\mathrm{in}}e^{i3\varphi} + ... \\ &= -rE_{\mathrm{in}} + rt^2E_{\mathrm{in}}e^{i\varphi}\sum_{q=0}^{\infty}(r^2e^{i\varphi})^q = \\ &= rE_{\mathrm{in}}\left(\frac{(r^2+t^2)e^{i\varphi}-1}{1-r^2e^{i\phi}}\right) \end{aligned} \tag{2.26}$$

Likewise, the sum of the transmitted beams E_{trans} is

$$\begin{aligned} E_{\mathrm{trans}} &= t^2E_{\mathrm{in}} + r^2t^2E_{\mathrm{in}}e^{i\varphi} + r^4t^2E_{\mathrm{in}}e^{i2\varphi} + ... \\ &= t^2E_{\mathrm{in}}\sum_{q=0}^{\infty}(r^2e^{i\varphi})^q = \\ &= \frac{t^2E_{\mathrm{in}}}{1-r^2e^{i\varphi}} \end{aligned} \tag{2.27}$$

The reflection coefficient $F(\omega)$ can be described as

$$\begin{aligned} F(\omega) &= \frac{E_{\text{ref}}}{E_{\text{in}}} = \\ &= r\left(\frac{t^2 e^{i\varphi}}{1 - r^2 e^{i\varphi}} - 1\right) \end{aligned} \tag{2.28}$$

where $\varphi = \dfrac{\omega}{\nu_{\text{FSR}}}$.

If the losses due to absorption are neglected, the transmission $T = t^2$ and reflection $R = r^2$ follows the relation $R + T = 1$. Then the intensity of the reflected beam I_{ref} is

$$\begin{aligned} I_{\text{ref}} &= |E_{\text{ref}}|^2 = \\ &= I_0 r^2 \left|\frac{(e^{i\varphi} - 1)}{1 - r^2 e^{i\varphi}}\right|^2 = \\ &= I_0 \frac{4r^2 \sin^2\left(\frac{\varphi}{2}\right)}{(1 - r^2)^2 + 4r^2 \sin^2\left(\frac{\varphi}{2}\right)} = \\ &= I_0 \frac{4R \sin^2\left(\frac{\varphi}{2}\right)}{(1 - R)^2 + 4R \sin^2\left(\frac{\varphi}{2}\right)} \end{aligned} \tag{2.29}$$

From the intensity of the reflected beam it follows that the intensity of the transmitted beam is

$$I_{\text{trans}} = 1 - I_{\text{ref}} = I_0 \frac{(1 - R)^2}{(1 - R)^2 + 4R \sin^2\left(\frac{\varphi}{2}\right)} \tag{2.30}$$

if the losses can be ignored.

2.2.2 Finesse

The finesse of a cavity is defined as

$$\mathcal{F} = \frac{\pi\sqrt{R}}{1 - R} \tag{2.31}$$

and only depends on the reflectivity of the mirrors. Inserting the finesse into equation (2.29), the reflected beam becomes

$$I_{\text{ref}}(\nu) = \frac{I_0 \sin^2\left(\dfrac{\pi\nu}{\nu_{\text{FSR}}}\right)}{\left(\dfrac{\pi}{2\mathcal{F}}\right)^2 + \sin^2\left(\dfrac{\pi\nu}{\nu_{\text{FSR}}}\right)}. \tag{2.32}$$

and inserting the finesse (2.31) into equation (2.30), the transmitted beam becomes

$$I_{\text{trans}}(\nu) = \frac{I_0}{1 + \left(\dfrac{2\mathcal{F}}{\pi}\right)^2 \sin^2\left(\dfrac{\pi\nu}{\nu_{\text{FSR}}}\right)} \tag{2.33}$$

The maximum transmitted intensity $I_{\max}$ is achieved when the frequency is an integer multiple of the free spectral range ν_{FSR}. Near resonance, the sine part of equation (2.33) tends to $\left(\frac{\pi\nu}{\nu_{\mathrm{FSR}}}\right)^2$ and equation (2.33) becomes a Lorentzian

$$I_{\mathrm{trans}}(\nu) = \left(\frac{\nu_{\mathrm{FSR}}}{2\mathcal{F}}\right)^2 \frac{I_{\max}}{\nu^2 + \left(\frac{\nu_{\mathrm{FSR}}}{2\mathcal{F}}\right)^2}. \tag{2.34}$$

The full width at half maximum (FWHM) of the Lorentzian resonance line is

$$\Delta\nu_c \approx \frac{\nu_{\mathrm{FSR}}}{\mathcal{F}} \tag{2.35}$$

The finesse of a cavity can be determined by a ring-down measurement as in section 3.1.3.

2.2.3 Pound–Drever–Hall technique

The Pound–Drever–Hall (PDH) technique is a common way of stabilising the frequency of a laser. It is a technique used to lock a laser to a Fabry-Pérot cavity. (The technique is similar to a method used for frequency stabilisation of microwave oscillators developed by R.V. Pound in the 1940s) [11]. Figure 2.8 shows a schematic of a PDH setup. The laser light is phase modulated for example by using an EOM which gets a signal from a local oscillator (LO). The frequency spectrum of the light then consists of a carrier signal and two sidebands. The light is sent to a cavity, and the light reflected by the cavity is reflected onto a photo diode (PD) by a polarising beam splitter (PBS). The photodiode signal is multiplied with the signal from the same local oscillator used for the modulation in a mixer. The signal from the mixer is filtered using a low pass filter and and the filtered signal provides the error signal for the feedback loop. The error signal describes how far the carrier is off resonance with respect to the cavity and is used to provide feedback to the system using a PID controller (See section 2.3.1).

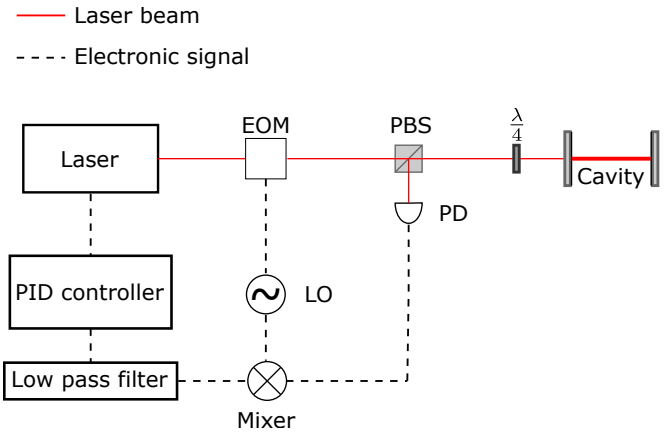

Figure 2.8: A schematic representation of a PDH setup.

The mathematical description of the technique follows E.D. Black (2001) [11]. The phase modulated laser beam can be described as

$$E_{\text{in}} = E_0 e^{i(\omega t + \beta \sin(\Omega_{\text{mod}} t))} \tag{2.36}$$

Where β is the modulation depth and Ω_{mod} is the frequency of the modulation. For $\beta \ll 1$ equation (2.36) can be expanded to the first order using Bessel functions of the first kind J_n

$$\begin{aligned} E_{\text{in}} &\approx E_0 e^{i\omega t} \left[J_0(\beta) + 2iJ_1(\beta)\sin(\Omega_{\text{mod}} t)\right] = \\ &= E_0 \left[J_0(\beta)e^{i\omega t} + J_1(\beta)e^{i(\omega+\Omega_{\text{mod}})t} - J_1(\beta)e^{i(\omega-\Omega_{\text{mod}})t}\right] \end{aligned}$$

Assuming the incident intensity is constant, the total power of the incident beam can be defined as $P_0 \equiv |E_0|^2$. The power in the carrier is

$$P_{\text{c}} = J_0(\beta)^2 P_0 \tag{2.37}$$

and the power in each first-order sideband becomes

$$P_{\text{s}} = J_1(\beta)^2 P_0 \tag{2.38}$$

For small modulation depths ($\beta < 1$), the power is almost exclusively in the carrier and the first-order sidebands. Then the total reflected electric field is

$$\begin{aligned} E_{\text{ref}} = E_0 \big[&F(\omega)J_0(\beta)e^{i\omega t} + \\ &+ F(\omega+\Omega_{\text{mod}})J_1(\beta)e^{i(\omega+\Omega_{\text{mod}})t} - F(\omega-\Omega_{\text{mod}})J_1(\beta)e^{i(\omega-\Omega_{\text{mod}})t}\big] \end{aligned} \tag{2.39}$$

Where F is the reflection coefficient from equation (2.28). The power in the

reflected beam is $P_{\text{ref}} = |E_{\text{ref}}|^2$

$$\begin{aligned} P_{\text{ref}} = {} & P_{\text{c}} |F(\omega)|^2 + P_{\text{s}}\{|F(\omega+\Omega_{\text{mod}})|^2 + |F(\omega-\Omega_{\text{mod}})|^2\}+ \\ & + 2\sqrt{P_{\text{c}}P_{\text{s}}}\{\text{Re}\left[F(\omega)F^*(\omega+\Omega_{\text{mod}}) - F^*(\omega)F(\omega-\Omega_{\text{mod}})\right]\cos(\Omega_{\text{mod}}t)+ \\ & + \text{Im}\left[F(\omega)F^*(\omega+\Omega_{\text{mod}}) - F^*(\omega)F(\omega-\Omega_{\text{mod}})\right]\sin(\Omega_{\text{mod}}t)\}+ \\ & + \mathcal{O}(2\Omega_{\text{mod}}) \end{aligned} \tag{2.40}$$

The terms in the equation above arise from adding three waves of different frequencies, the carrier ω and the two sidebands $\omega \pm \Omega_{\text{mod}}$. The terms oscillating with Ω_{mod} originate from the carrier interfering with the left and right sideband. The $2\Omega_{\text{mod}}$ term comes from the sidebands interfering with each other. The two terms that oscillate at the modulation $\sin(\Omega_{\text{mod}}t)$ and $\cos(\Omega_{\text{mod}}t)$ are of interest since they contain the phase information of the reflected carrier signal. By using a mixer and a low-pass filter, these oscillating terms can be isolated. The mixer will form a product of its inputs which means that in the case of two sine waves the output of the mixer is

$$\sin(\Omega_{\text{mod}}t)\sin(\Omega' t) = \frac{1}{2}\{\cos\left[(\Omega_{\text{mod}} - \Omega')t\right] - \cos\left[(\Omega_{\text{mod}} + \Omega')t\right]\} \tag{2.41}$$

where Ω_{mod} is the modulation signal and Ω' is the reference. If $\Omega_{\text{mod}} \simeq \Omega'$ (which is the interesting case) the $\cos\left[(\Omega_{\text{mod}} - \Omega')t\right]$ term will be a low-frequency signal that will pass through a following low-pass filter, while the $\cos\left[(\Omega_{\text{mod}} + \Omega')t\right]$ part will be filtered out. In the case of mixing a sine with a cosine the output of the mixer is

$$\sin(\Omega_{\text{mod}}t)\cos(\Omega' t) = \frac{1}{2}\{\sin\left[(\Omega_{\text{mod}} - \Omega')t\right] - \sin\left[(\Omega_{\text{mod}} + \Omega')t\right]\} \tag{2.42}$$

when $\Omega_{\text{mod}} = \Omega'$ the low-frequency signal vanishes. For low modulation frequencies the signals going into the mixer must be in phase with each other in order to observe a signal i.e. a sine with a sine and a cosine with cosine. In reality, this is true even for high modulation frequencies, since any delay in one of the signals will cause a phase shift which distorts the output signal of the mixer. Therefore the phase of the two signals is analysed and matched before the mixer. In equation 2.40 the imaginary part will give a larger slope around $\Omega_{\text{mod}} \simeq \Omega'$ compared to the real part and therefore the imaginary part is more suitable for the error signal. The remaining signal consists of the sine term of equation (2.40)

$$\epsilon = 2\sqrt{P_{\text{c}}P_{\text{s}}}\text{Im}\{F(\omega)F^*(\omega+\Omega_{\text{mod}}) - F^*(\omega)F(\omega-\Omega_{\text{mod}})\} \tag{2.43}$$

This is known as the PDH error signal. Figure 2.9 shows the error signal as a function of the frequency detuning with $\nu_{\text{FSR}} = 1$ GHz for $\mathcal{F} = 1,000$ and $\mathcal{F} = 10,000$. The error signal correspond to the cavity response of laser frequency fluctuations in terms of reflected and transmitted optical power, where the locking point is the zero-crossing of the slope between the peak and the dip

of the carrier part of the signal. As shown in figure 2.9b, the gradient of the slope between the peak and the dip depends on the finesse. Since a steeper slope will generate a larger cavity response to a small laser frequency shift the sensitivity of the lock depends on the steepness of the slope. Therefore a higher finesse of the cavity enables a more accurate lock of the laser frequency.

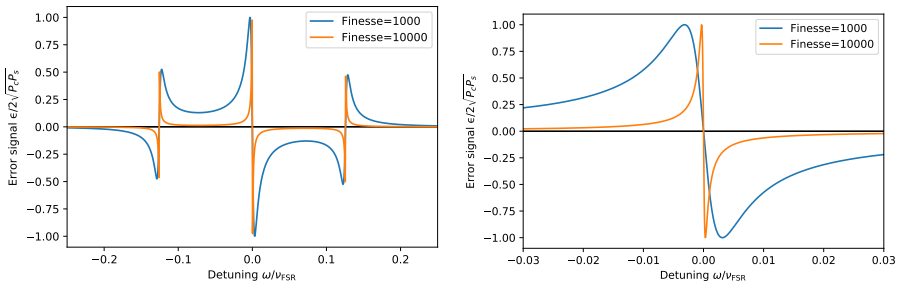

(a) **(b)**

Figure 2.9: The theory curve of the error signal (equation (2.43)) as a function of the frequency detuning for $\mathcal{F} = 1,000$ (blue) and $\mathcal{F} = 10,000$ (orange) with parameters $\nu_{\mathrm{FSR}} = 1$ GHz and $\Omega_{\mathrm{mod}} = 2\pi \times 20$ MHz, where **(b)** is a zoomed-in version of **(a)** near the resonance.

If the carrier is near-resonant and the sidebands are modulated at a frequency much larger than the cavity linewidth one can assume that the sidebands are totally reflected, $F(\omega \pm \Omega) \approx -1$ then

$$F(\omega)F^*(\omega+\Omega) - F^*(\omega)F(\omega-\Omega) \approx -2i\mathrm{Im}\{F(\omega)\} \tag{2.44}$$

This gives

$$P_{\mathrm{ref}} \approx 2P_{\mathrm{s}} - 4\sqrt{P_{\mathrm{c}}P_{\mathrm{s}}}\mathrm{Im}\{F(\omega)\}\sin(\Omega t) \tag{2.45}$$

Since the carrier is near-resonant

$$\frac{\omega}{\nu_{\mathrm{FSR}}} = 2\pi q + \frac{\delta\omega'}{\nu_{\mathrm{FSR}}} \tag{2.46}$$

where q is an integer and $\delta\omega'$ is the frequency deviation of the laser from the resonance. The approximation $\mathcal{F} = \pi/(1-r^2)$ can be made by assuming that the finesse of the cavity is high. Using equation for the cavity linewidth (2.35) the reflection coefficient F becomes

$$F \approx \frac{i}{\pi}\frac{\delta\omega'}{\Delta\nu_c} \tag{2.47}$$

For $\delta\omega' \ll \Delta\nu_c$ the error signal is approximately

$$\epsilon \approx -\frac{4}{\pi}\sqrt{P_{\mathrm{c}}P_{\mathrm{s}}}\frac{\delta\omega'}{\Delta\nu_c} \tag{2.48}$$

From equation (2.48) as well as in figure 2.9 it is shown that ϵ depends linearly on the frequency deviation $\delta\omega'$, ϵ depends on the cavity linewidth and the power.

2.3 Control systems

2.3.1 The Proportional-Integral-Derivative controller

A Proportional-Integral-Derivative (PID) controller is used to apply feedback to a process and consists of three terms, the proportional (P), the integral (I) and the derivative (D). As shown in figure 2.10, a reference signal $r(t)$ which is the desired set-point of the process is fed to the control system. The reference signal together with the process variable $y(t)$ which is the sensed position of the process creates the error signal $e(t) = r(t) - y(t)$. The error signal is used to derive three correction terms P, I and D. The sum of P, I and D is used to adjust the process via control variable $u_c(t)$. The process reacts on $u_c(t)$ which gives a new $y(t)$ and the control loop is complete [12]. The control actions of the three terms P, I and D are described below:

- The proportional term gives a correction proportional to the error signal and the manipulated control variable is

$$u_{\mathrm{P}}(t) = k_{\mathrm{P}} e(t) \tag{2.49}$$

  where k_{P} is the proportional gain. The term is proportional to the gain of the controller i.e. a large value of the proportional gain gives a large output response.

- The integral term gives a correction proportional to the integral of the error signal, therefore the control variable is

$$u_{\mathrm{I}}(t) = k_{\mathrm{I}} \int_{-t}^{t} e(t')dt' \tag{2.50}$$

  where k_{I} is the integral gain. The term is proportional to the magnitude and the duration of the error. This speeds up the set-point adjustment of the system.

- The derivative term gives a correction proportional to the time-derivative of the error signal, therefore the control variable is

$$u_{\mathrm{D}}(t) = k_{\mathrm{D}} \frac{de(t)}{dt} \tag{2.51}$$

  where k_{D} is the derivative gain. The term calculates the slope of the error and therefore it predicts the system behaviour over time. This speeds up the response of the controller, because a fast change in the error will give a fast response of the controller.

Therefore the total control variable $u_c(t)$ which gives the control action of the controller is

$$u_c(t) = k_{\mathrm{P}} e(t) + k_{\mathrm{I}} \int_{-t}^{t} e(t')dt' + k_{\mathrm{D}} \frac{de(t)}{dt} \tag{2.52}$$

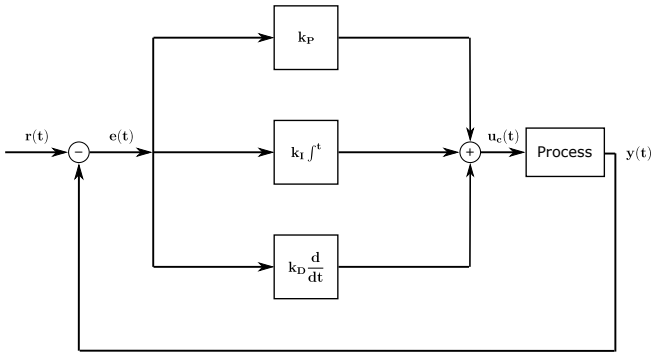

Figure 2.10: A block diagram of a PID controller.

The PID transfer function in the Laplace domain is

$$\begin{aligned} L(s) &= k_P + \frac{k_I}{s} + \frac{k_D s}{s+p} \\ &= \frac{(k_P + k_D)s^2 + (k_P p + k_I)s + k_I p}{s^2 + sp} \end{aligned} \tag{2.53}$$

The p in the derivative part of the transfer function is a low-pass filter to avoid high-frequency noise to propagate through the controller. Since the derivative term enables a quick response to a quick change in the system [12]. Figure 2.11 shows the Bode phase plot of a PID controller. A Bode phase plot describes the phase shift of the frequency response of a system. In figure 2.11 the non-zero values of k_P, k_I and k_D are $k_P = k_I = k_D = 0.5$.

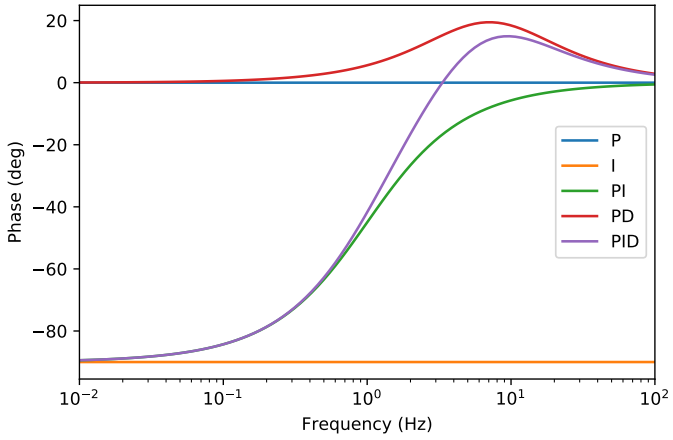

Figure 2.11: A Bode phase plot of a P, I, PI, PD and PID controller with the characteristic frequency $\omega_c = 4000\pi$ Hz. When k_P, k_I and k_D are non-zero $k_P = k_I = k_D = 0.5$.

In this thesis a PID controller was used as a part of the feedback loop used to

lock the laser to a high finesse cavity in the PDH setup. The setup is described in section 3.1.1. A PID controller was also used to stabilise the temperature of the cavity, as described in section 3.1.5.

Chapter 3

Experimental results

3.1 Laser frequency stabilisation and characterisation

In the trapped ion experiment there are two laser setups, the old 674 nm laser (674 laser I) which is locked to the old cavity (cavity I) and the new 674 nm laser (674 laser II) which is locked to the new cavity (cavity II). In this thesis the 674 laser II system is set up and the 674 laser II is characterised. Figure 3.1 shows the setup of the 674 laser II system. The 674 laser II is a diode laser at 674 nm from Toptica that arrived on the 2$^{\text{nd}}$ of May 2019. As shown in figure 3.2 the laser consists of a laser diode, an electro-optic modulator (EOM) and a grating. The diode, EOM and grating are all inside a cavity. The EOM was placed inside the cavity to reduce servo-bumps. A beam splitter (BS) splits the light from the laser cavity into one part that can be used directly and the other part is guided by mirrors to a tapered amplifier (TA) that amplifies the intensity of the light. Two optical isolators (OI) are also used to block back-reflected light from hitting the diode or the TA. Cavity II is an ultra-stable high-finesse optical reference cavity from Menlo Systems that arrived on the 29$^{\text{th}}$ of April 2019. It has a cavity spacer made of ultra-low expansion (ULE) glass with a linear shrinking drift rate of approximately 0.15 Hz/s and mirror surfaces made out of fused silica. The cavity is situated inside a vacuum chamber (shown in figure 3.1b) to further reduce environmental effects. The cavity finesse specified by the company is $> 200,000$ and the cavity length is $L = 121$ mm.

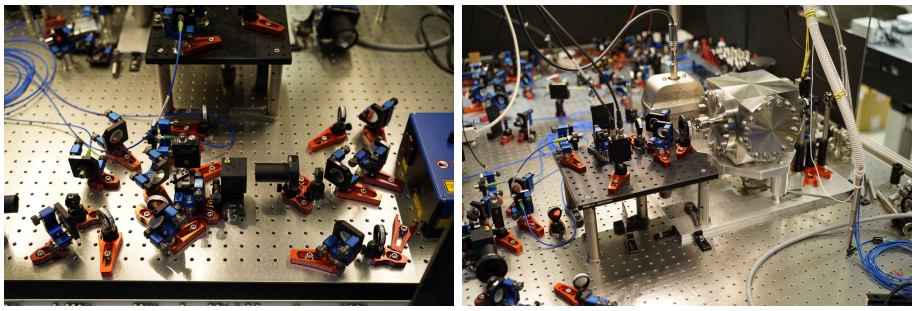

(a) (b)

Figure 3.1: Pictures of the 674 laser II and cavity II setup **(a)** shows the setup after the 674 laser II and **(b)**shows the vacuum chamber of cavity II and the setup before the cavity.

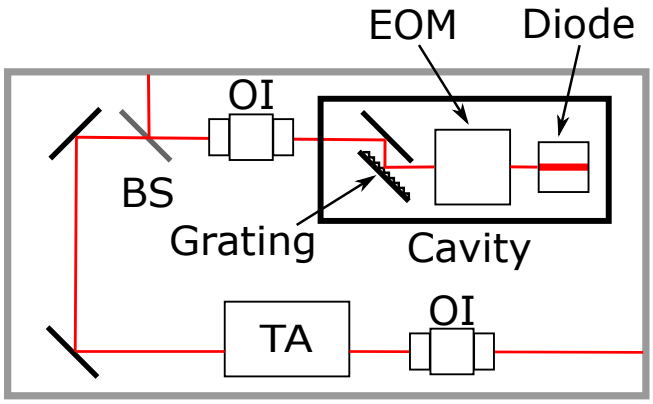

Figure 3.2: A schematic of the 674 laser II.

3.1.1 The Pound-Drever-Hall signal

The PDH signal was generated using the setup shown in figure 3.3. The setup uses the light from the 674 laser II (for more details on the laser see section 3.1) before the tapered amplifier (TA) and therefore the light after the TA was blocked. The light emitted by the laser goes through a $\frac{\lambda}{2}$ wave-plate and a Glan-Thompson polariser (GT) to ensure clean linear polarisation. Then the light goes through an electro-optic modulator (EOM) which generates the sidebands at the drive frequency of the signal and is guided through a single-mode fiber to the cavity setup. In the cavity setup the light enters cavity II and the reflected light is directed to the photodiode (PD1) via a polarising beam splitter (PBS). The PD signal is sent to the mixer. The mixer also takes a reference signal from a local oscillator and produces the error signal used in the PID controller (Toptica FALC) that provides the feedback to the laser.

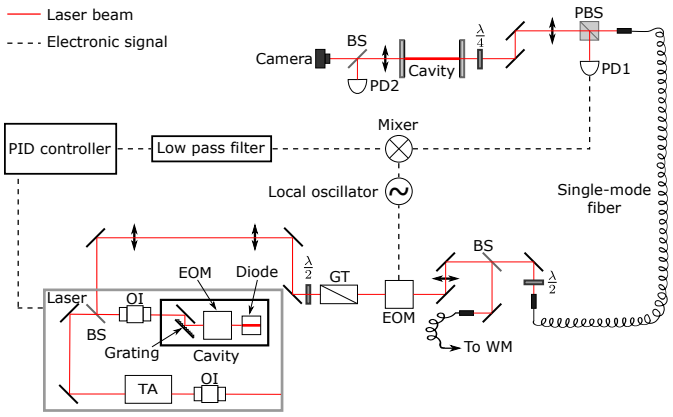

Figure 3.3: A schematic of the laser frequency stabilisation setup.

Figure 3.4 shows the measured PDH error signal and the DC-component of the photodiode signal in reflection. The sidebands in the figures correspond to the driving frequency of the EOM at ±19.44 MHz when scanning the voltage of the piezo of the laser grating over the resonance of the cavity. The sidebands in the reflection signal in Figure 3.4b are roughly 7% of the carrier dip for the left dip and 6% of the carrier dip for the right dip. This means that

$$\frac{P_\mathrm{s}}{P_\mathrm{c}} = \frac{J_1(\beta)^2 P_0}{J_0(\beta)^2 P_0} = \frac{J_1(\beta)^2}{J_0(\beta)^2} \simeq 0.06 \tag{3.1}$$

the modulation depth β is small and can be approximated as

$$\beta \simeq \frac{1}{2}\frac{J_1(\beta)}{J_0(\beta)} = \frac{\sqrt{0.06}}{2} \approx 0.1 \tag{3.2}$$

The experimental data in figure 3.4 resembles the theory signal plotted in figure 2.9.

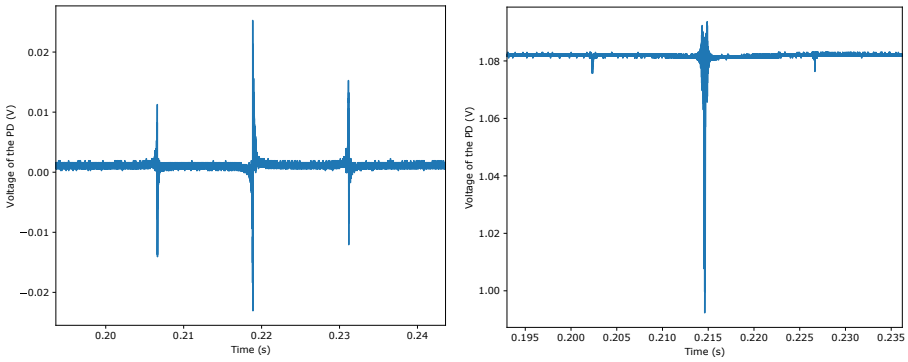

(a) **(b)**

Figure 3.4: **(a)** The PDH error signal with sidebands corresponding to ±19.44 MHz frequency offset when scanning the voltage of the piezo of the laser grating over the resonance of the cavity. **(b)** The low-frequency component of the photodiode signal in reflection (the RF-component is sent to the mixer). The left sideband is roughly 7% of the carrier dip and the right sideband is 6% of the carrier dip.

3.1.2 The free spectral range

The free spectral range (FSR) of the cavity was measured using the 674 laser II locked to different TEM_{00}-modes of cavity II. The frequency of the laser was measured using the wavelength meter(High Finesse WS6-200). Then the laser frequency was changed to the next TEM_{00}-mode, the laser was locked again and the measurement was repeated for this mode. From the slope of the fitted data points plotted in figure 3.5 the ν_{FSR} was determined

$$\nu_{\mathrm{FSR}} = (1.241 \pm 0.003)\ \mathrm{GHz} \tag{3.3}$$

The wavelength meter has a specified absolute accuracy of < 200 MHz. Each measurement was performed by first calibrating the wavelength meter with 674 laser I, then take a set of measurements using a single mode fiber coupled to the wavelength meter without a fiber switch, reading out the wavelength meter via a USB to obtain more digits and then averaging. Calculating the FSR of cavity II using equation (2.23) with the cavity length specified by the company with $L = 121$ mm gives $\nu_{\mathrm{FSR}} \approx 1.239$ GHz, this is consistent with the measured FSR.

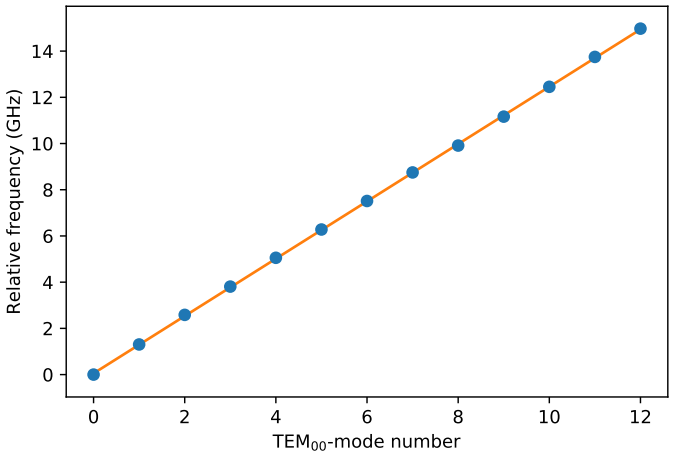

Figure 3.5: The relative frequency change as a function of mode number with errorbars at 200 MHz which is the upper limit for the specified absolute accuracy of the wavelength meter, this is too small to be visible in this plot. The slope corresponds to a $\nu_{\mathrm{FSR}} = (1.241 \pm 0.003)$ =GHz.

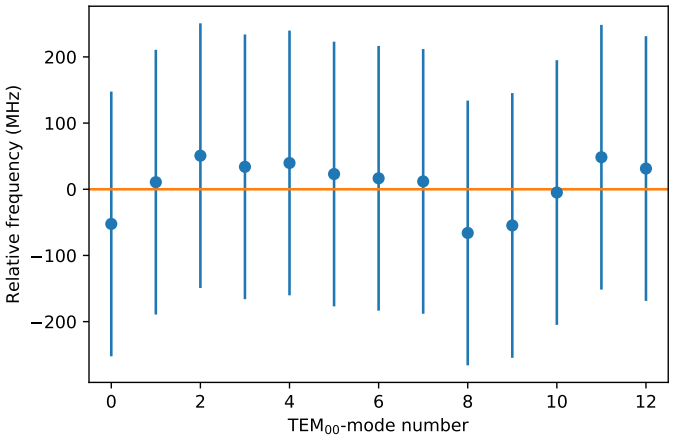

Figure 3.6: The same plot as in figure 3.5 when subtracting the slope, with same the errorbars at 200 MHz. The root mean square of the measurement is $\nabla_{\mathrm{RMS}} = 40$ MHz.

The errorbars for the data points in figure 3.5 are at 200 MHz and are therefore not visible in the plot. They are the upper limit for the specified absolute accuracy of the wavelength meter. However, the uncertainties obtained by taking several measurements of the same point and then use the standard deviation of the measurements were on the order of 800 kHz, this corresponds to the precision of the measurement. The accuracy of the measurement, however is limited by the calibration of the wavelength meter. Figure 3.6 shows the FSR

measurement when subtracting the slope in figure 3.5. As shown in figure 3.6 there is some scattering with a root mean square of $\nabla_{\mathrm{RMS}} = 40$ MHz which seems to be the accuracy of the measurement. This might explain why the standard deviation of the set of measurements for each datapoint is much smaller than the uncertainty in the FSR measurement.

3.1.3 Determining the cavity linewidth using a ring-down measurement

The light field decay time can be measured by first sending light into the cavity and then blocking the light going to the cavity while recording the transmission signal. The light inside the cavity and thus the light transmitted by the cavity decays exponentially as

$$I = I_0 e^{-t/\tau} \tag{3.4}$$

where I_0 is the initial intensity, t is the time and τ is the cavity decay time. From the cavity decay time the cavity linewidth $\Delta\nu_c$ follows

$$\Delta\nu_c = \frac{1}{2\pi\tau} \tag{3.5}$$

When this measurement was taken the lock to cavity II of the 674 laser II was still very unstable. Therefore this experiment was performed using laser light derived from the 674 laser I, which was locked to cavity I to ensure stability of the laser lock. Some light from the 674 laser I was sent to cavity II. By using several acousto-optical modulators (AOMs), the frequency of the light was adjusted to match the frequency of the TEM_{00}-mode of cavity II. One of the AOMs was used to switch off the light going to the cavity and the transmission signal was measured using a photodiode (PD2 in figure 3.3). The photon decay-time τ of the cavity was determined by fitting the exponential in figure 3.7 to equation (3.4). By taking multiple sets of the cavity ring-down measurement the averaged result of the photon decay time was

$$\tau = (5.13 \pm 0.15)\ \mu\mathrm{s} \tag{3.6}$$

The result was then used to calculate the cavity linewidth using equation (3.5) and the finesse using equation (2.35) the results were

$$\Delta\nu_c = (30,700 \pm 800)\ \mathrm{Hz}$$
$$\mathcal{F} = (40,000 \pm 1,000)$$

The finesse stated by the company was $> 200,000$, which is significantly higher than $40,000$. This means that the reflectivity of the mirrors is lower than promised either due to absorption in the mirror coatings or due to scattering losses for instance by dust on the mirrors. A consequence of a low finesse is that the achievable locked-laser linewidth is broader. Therefore the cavity will be sent back to the company for testing.

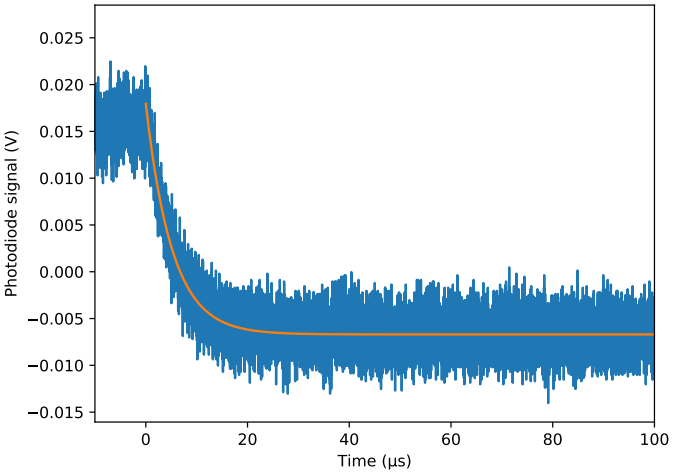

Figure 3.7: The ringdown measurement of cavity II.

3.1.4 Measurement of the cavity linewidth using the signal of the transmission photodiode.

As a consistency check, the cavity linewidth was measured using a different method. For the same reasons as in section 3.1.3 the 674 laser I was used to ensure stability of the laser lock. Figure 3.8 shows the signal of the transmission photodiode (PD2) when scanning the laser frequency over the resonance of the TEM_{00}-mode of cavity II using an AOM. The data was fitted to a Lorentzian function (see equation (2.34)) and the linewidth obtained was $(34,700 \pm 200)$ Hz. This is slightly broader than the linewidth obtained from the ring-down measurement which may be explained by the fact that this measurement is more sensitive to laser frequency noise that causes the linewidth to be overestimated.

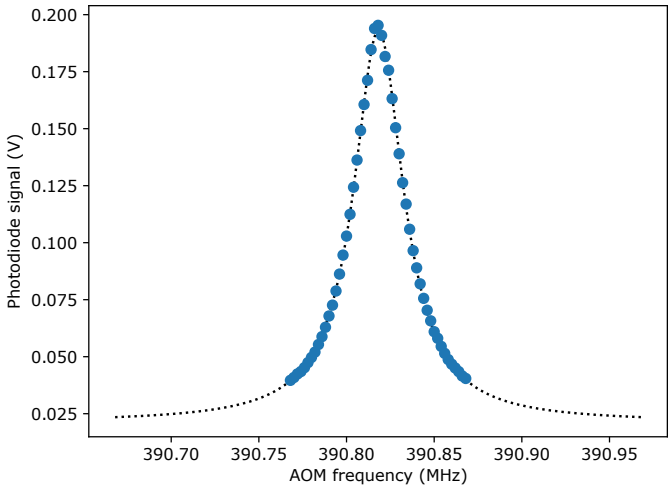

Figure 3.8: Scanning the laser frequency over the resonance of the TEM_{00}-mode of cavity II.

3.1.5 Stabilising the temperature of the cavity

The cavity was placed inside a vacuum chamber to isolate it from the environment. In order to control the temperature, the cavity was connected to a Peltier element and two temperature sensors (NTC thermistors) inside the vacuum chamber. The Peltier element and the two temperature sensors were connected to a temperature controller (SRS PTC10) using a foil-shielded twisted pair cable to reduce noise and cross-talk between the cables (For more information see the appendix). In this setup the Peltier element is used for adjusting the temperature of the cavity, effectively converting an applied current from the temperature controller to a heating or cooling of the cavity. The temperature sensors are used for measuring the temperature effectively giving feedback to the temperature controller. The temperature controller used a PID control loop for the feedback (See section 2.3.1). Figure 3.9 shows the response of the temperature controller for different values of P, I and D.

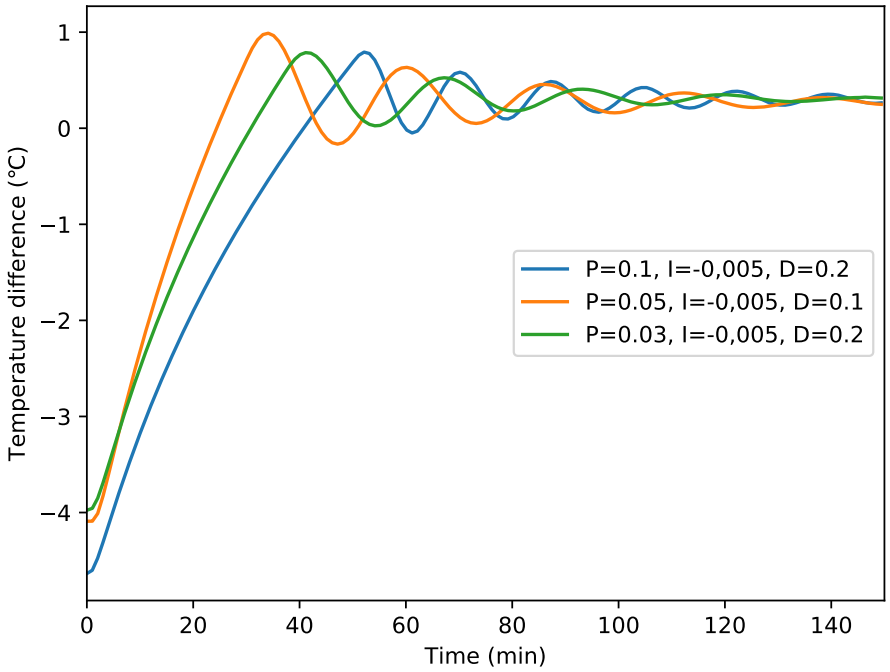

Figure 3.9: The normalised response of the temperature controller when changing the temperature as a function of time for different values of P, I and D.

As shown in figure 3.9 they are all slightly underdamped, but the response function still overshoots a little and stabilises quite well after that. It was difficult to find a response function that was not either underdamped or overdamped, but still stabilises within the same time as the functions shown in figure 3.9.

3.1.6 The zero-expansion-point of the cavity

When a laser is locked to a cavity, the stability of the length of the cavity is transferred to the stability of the laser frequency. Temperature fluctuations can cause instability in the length of a cavity as the cavity material expand or shrink with changes in temperature. The coefficient of thermal expansion (CTE) of the cavity describes the changes in length of the cavity with a change in temperature. For reference cavities, the cavity spacer is made of ultra-low expansion glass with a CTE close to zero. Mirrors are optically contacted to avoid thermal expansion of any glue. The zero-expansion-point (ZEP) is the temperature at which the CTE of the cavity is zero and therefore the temperature fluctuations at that point have the smallest effect on the length of the cavity. This experiment used the same type of setup as the one described in section 3.1.3, where laser light derived from the 674 laser I, which was locked to cavity I to ensure stability of the laser lock. The frequency of the light was adjusted to match the frequency of the TEM_{00}-mode of cavity II by using several AOMs and then the

frequency of the light was measured by the wavelength meter. After measuring the frequency of the light, the temperature was adjusted to a new set-point. The next measurement of the frequency of the light at the new set-point was taken several hours after the previous one to allow the system to stabilise at the new temperature. The measurement was repeated for different temperatures and the results are plotted in figure 3.10. The result of the measurements can be described by the following parabolic function $\nu = A(T - T_0)^2 + B$. The coefficients A, B and T_0 were determined from the fit of the datapoints plotted in figure 3.10

$$A = (0.14 \pm 0.02)\ \mathrm{MHz}/^\circ\mathrm{C}^2$$
$$B = (406.9 \pm 0.3)\ \mathrm{MHz}$$
$$T_0 = (33.0 \pm 0.2)\ ^\circ\mathrm{C}$$

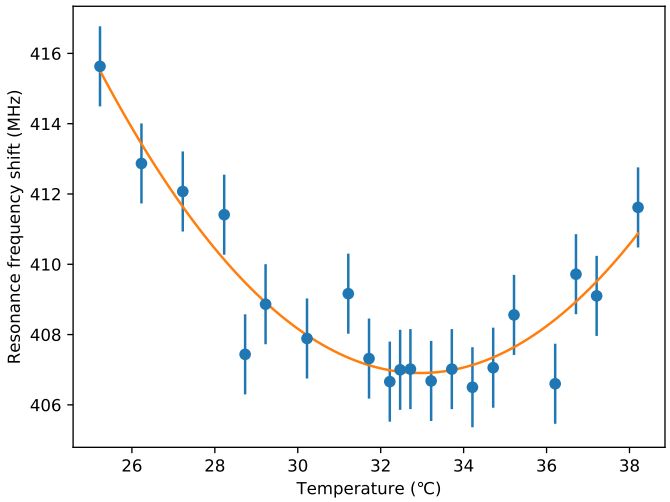

Figure 3.10: Measurement of the zero expansion point of the cavity.

3.1.7 The linewidth of the locked laser

An upper bound for the linewidth of the locked laser was determined by using a beat note between the 674 laser I and the 674 laser II shown in figure 3.11a. Each laser was locked to its respective cavity. The laser light from each laser was then frequency shifted using AOMs until their frequency difference was less than the detection bandwidth of the photodiode. Finally both lasers were sent onto the same photodiode. By taking multiple beat note measurements and then fitting each data set to a Lorentzian function the average linewidth of the beat note was (123 ± 6) Hz when the external modulation (used for stabilising 674 laser II) was applied to an external EOM. The linewidth was likely to be broadened by fiber noise since a 10 m fiber was used to send the 674 laser I light to the beat note setup which used part of the fiber noise cancellation setup that

Anders Lindberg built [8]. The beat note was also used to optimise lock of 674 laser II to cavity II. This was done by slowly adjusting the PID parameters of the 674 laser II PID controller (Toptica FALC) one at a time iteratively, while observing the changes in the beat note of the two lasers. Once the optimal parameters were found the lock of the cavity had become a lot more stable.

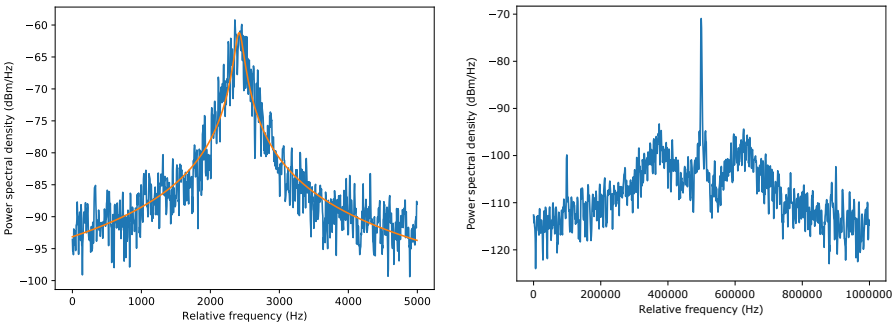

(a) **(b)**

Figure 3.11: **(a)** The beat note between the 674 laser I and the 674 laser II. **(b)** Shows a broader frequency range of the beat note where the servo bumps are visible.

Figure 3.11b shows the beat note in a broader frequency range where servo bumps are visible. The servo bumps are at 120 kHz away from the central frequency with 23 dBm/Hz amplitude difference compared to the central peak.

3.2 Experiments on the ion

Figure 3.12 show the schematic of the setup for sending light to the ion in lab 1. The first part of the setup is the same as described in section 3.1.1. For the light going to the ion, the light was amplified using a Tapered Amplifier (TA). The light is coupled into a short fiber and sent to a frequency shifting setup. There the light goes through a half wave-plate to ensure correct polarization, a PBS and an acousto-optic modulator (AOM). The frequency shift needed to match the frequency of the light going to the ion was roughly twice the optimal driving frequency of the AOM used. Therefore, the AOM was setup in a double-pass configuration. The +1st order light was reflected back through the AOM, then the subsequent 1st order was reflected on the PBS and sent through a fiber to lab 1.

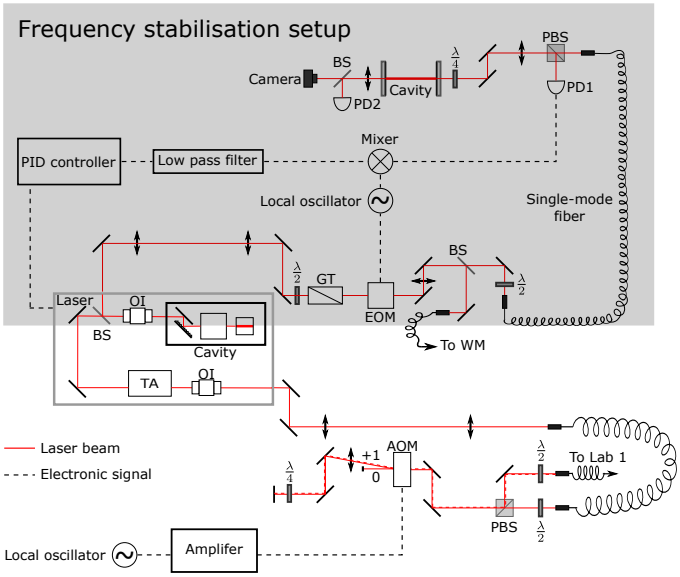

Figure 3.12: A schematic of the experimental setup for sending light to the ion in lab 1. The first part is the PDH setup in figure 3.3.

3.2.1 Frequency drifts of the cavity

The ion was used to measure the frequency drifts of the cavity. The transition $5S_{1/2} \leftrightarrow 4D_{5/2}$ of the ion should in principle remain the same in time as long as there are no drastic changes to the trap or the magnetic field experienced by the ion (See section 2.1). The changes in the magnetic field can be monitored by measurements on different Zeeman transitions. By making sure the trap is stable and taking the magnetic field fluctuations into account the transition $5S_{1/2} \leftrightarrow 4D_{5/2}$ can be used as a reference when measuring the frequency drifts of the cavity. The 674 laser II light was sent onto the ion using the setup described above. By using an AOM to adjust the frequency of the light to match the ion transition at different times, the drift of the cavity was measured. Figure 3.13 shows the results. The slope corresponds to a frequency drift rate of (306.9 ± 0.2) mHz/s.

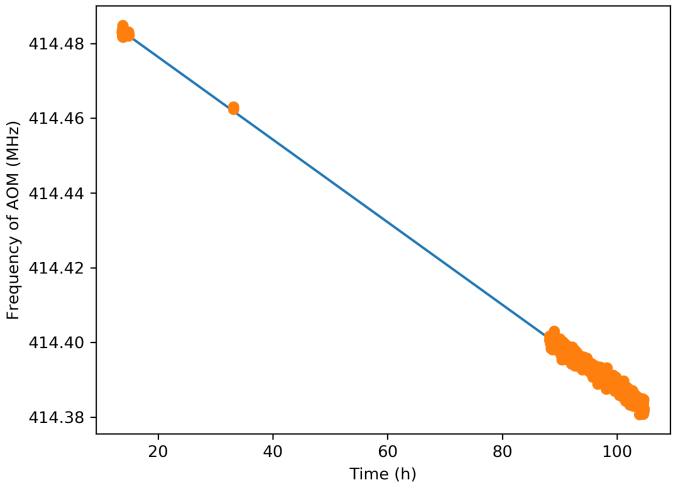

Figure 3.13: The frequency drift of the cavity measured using the ion transition $5S_{1/2} \leftrightarrow 4D_{5/2}$. The slope corresponds to the frequency drift rate is (306.9 ± 0.2) mHz/s.

3.2.2 Ramsey experiment

Coherence times for manipulation of ion qubits is limited by laser linewidth. To characterise the coherence time using the 674 laser II and cavity II setup a Ramsey experiment was performed. For the Ramsey experiment (for more information see section 2.1.5) transitions $5S_{1/2}(m_J = -1/2) \leftrightarrow 4D_{5/2}(m_J = -5/2)$ which is sensitive to the magnetic field strength and $5S_{1/2}(m_J = -1/2) \leftrightarrow 4D_{5/2}(m_J = -3/2)$ which is less sensitive to the magnetic field strength were used in order to distinguish between magnetic field fluctuations and laser frequency fluctuations. As described in the master thesis of Anders Lindberg [8]), the contrast decay will follow different distributions depending on the type of noise that causes the decoherence of the system. In this case the data plotted in figure 3.14 does not really fit an exponential decay. Instead, a Gaussian function $y = Ae^{-t^2/2\tau^2}$ was used to fit the data where τ is the coherence time. The measurements was done both with the line trigger and without the line trigger for comparison. The line trigger triggers the experiment on the line of the mains electricity, in order to reduce the oscillating B-field at the ion position caused by the oscillating current at the mains frequency (50Hz) from the appliances in the lab. The results of the experiment and the fits are plotted in figure 3.14.

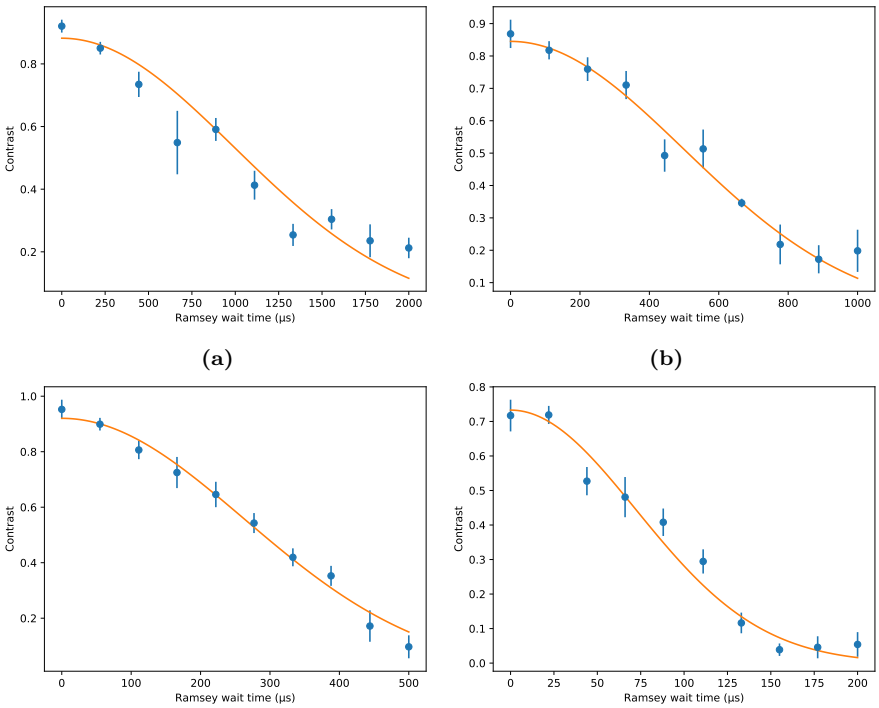

Figure 3.14: The contrast of the Ramsey measurements fitted to a Gaussian function of the less sensitive transition with line trigger (a), the sensitive transition with line trigger (b), the less sensitive transition without line trigger (c) and finally the sensitive transition without line trigger (d).

From the Gaussian fit the coherence times were determined and the results are plotted in figure 3.15. The coherence times were $\tau = (990 \pm 60)\,\mu$s for the less sensitive transition with line trigger, $\tau = (500 \pm 10)\,\mu$s for the sensitive transition with the line trigger, $\tau = (263 \pm 7)\ \mu$s for the less sensitive transition without line trigger and finally $\tau = (72 \pm 3)\ \mu$s for the sensitive transition without line trigger.

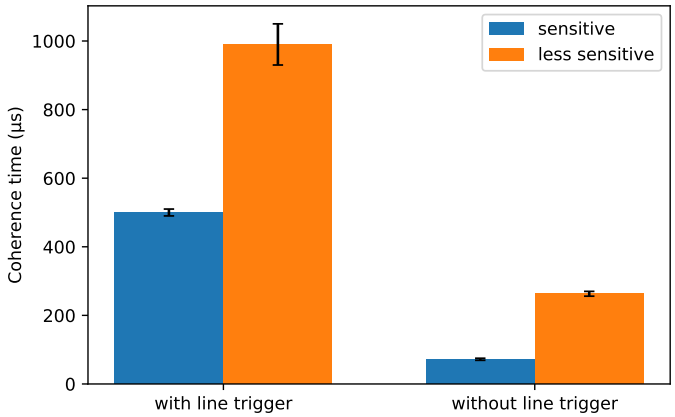

Figure 3.15: A comparison between the different coherence times for the sensitive transition (blue) and the less sensitive transition (orange) for both with and without the line trigger.

Comparing the results from figure 3.15 the coherence time for the transition that is sensitive to the magnetic field strength is much shorter than the coherence time for the transition that is less sensitive to the magnetic field strength. This indicates that the sources of decoherence is not dominated by the laser frequency fluctuations since the fluctuations should be the same for both transitions. This suggests that the limiting factor for a longer coherence time at the moment is the magnetic field fluctuations and not the laser frequency fluctuations. These results are also very similar to previous results by Anders Lindberg [8] using 674 laser I.

3.2.3 Rabi oscillations

Figure 3.16 shows the Rabi oscillations for both the 674 laser II and the 674 laser I on the carrier and the blue sidebands for the $5S_{1/2}(m_J = -1/2) \leftrightarrow 4D_{5/2}(m_J = -5/2)$ transition. The Lamb-Dicke parameter was calculated using equation (2.12) and for the settings used in the experiment the Lamb-Dicke parameter in the x-direction and in the y-direction are both $\eta \approx 0.04$.

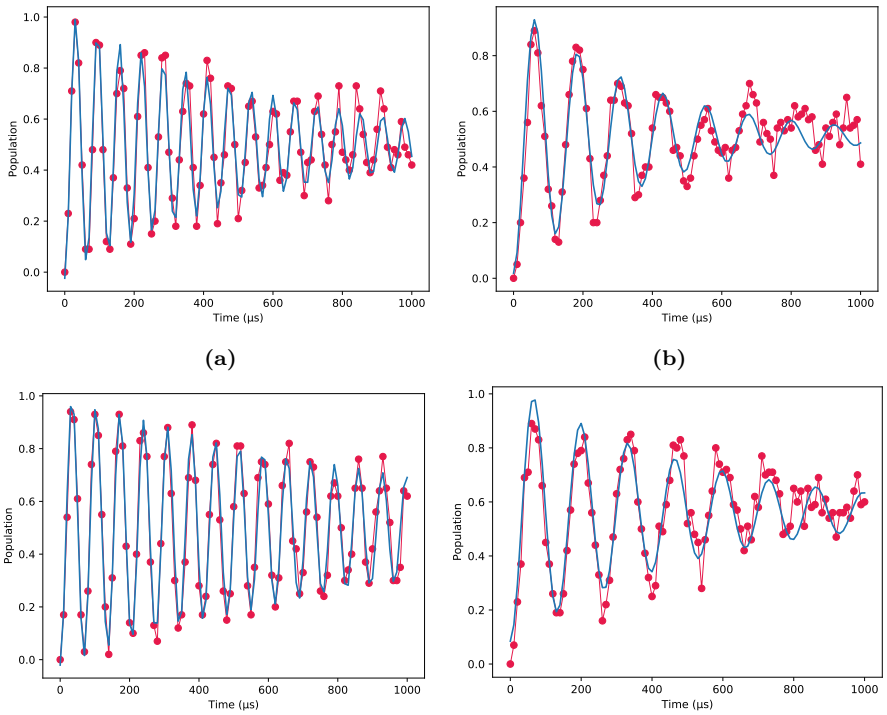

Figure 3.16: Comparing Rabi oscillations for the 674 laser II and the 674 laser I, a shows the Rabi oscillations on the carrier for 674 laser I, b shows the Rabi oscillations on the blue sideband for 674 laser I, c shows the Rabi oscillations on the carrier for 674 laser II and d shows the Rabi oscillations on the blue sideband for 674 laser II.

From the Rabi oscillations in figure 3.16 the coherence time could be determined. Figure 3.17 shows a comparison of the different coherence times for the carrier and blue sideband for both lasers.

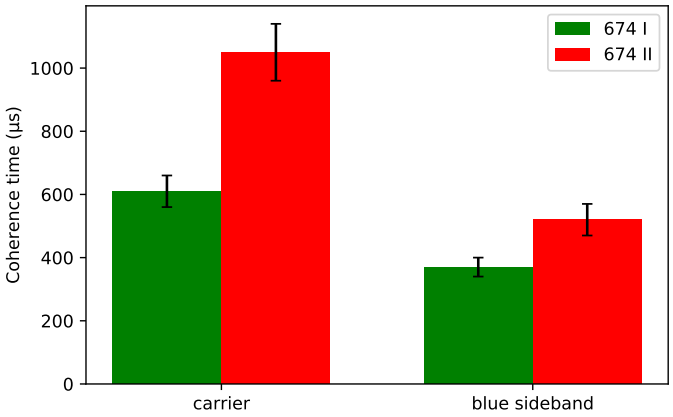

Figure 3.17: A comparison between the different coherence times for the 674 laser I (green) and the 674 laser II (red) for both the carrier and the blue sideband.

The coherence time for the respective cases are listed below.

- 674 laser I carrier coherence time (610 ± 50) μs
- 674 laser I blue sideband coherence time (370 ± 30) μs
- 674 laser II carrier coherence time $(1,050 \pm 90)$ μs
- 674 laser II blue sideband coherence time (520 ± 50) μs

The results show that the 674 laser II increased the coherence time compared to the 674 laser I. The coherence time for the 674 laser I is limited by its servo bumps, which could be a reason for the longer coherence time of the 674 laser II since the servo bumps of 674 laser II due to the intra cavity EOM should be at higher frequency and lower amplitude. This will open up new measurement possibilities since the servo bumps of 674 laser I has been a limiting factor.

3.2.4 Comparing the coherence times

Figure 3.18 shows the comparison between coherence time of the transition $5S_{1/2}(m_J = -1/2) \leftrightarrow 4D_{5/2}(m_J = -5/2)$ for both the Ramsey experiment and the Rabi oscillations. As shown in the figure there is a large discrepancy between the results, the coherence time for the Ramsey experiment is $\tau = (72 \pm 3)$ μs compared to $\tau = (1050 \pm 90)$ μs for the Rabi oscillations. Both measurements should give roughly the same result since it measures the coherence time for the same transition and the difference in measurement technique should not

affect the coherence time in this case. The cause of this discrepancy is still not understood. The initial investigations of possible causes including problems with the AOMs and the 674 nm laser beams have not revealed the answer. It is possible that the magnetic field fluctuations are averaged out by Rabi oscillations. Further investigations are needed, but this lies beyond the scope of this thesis.

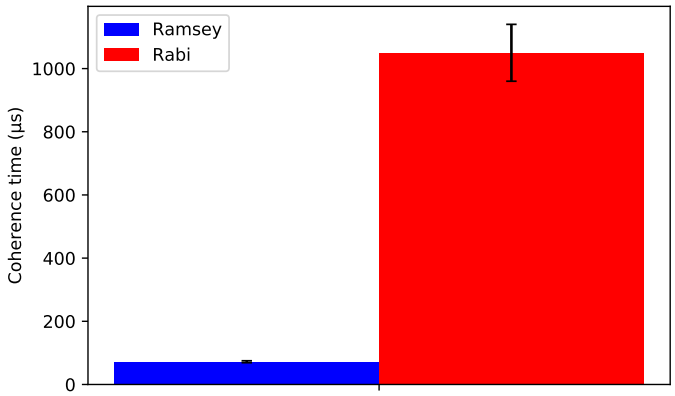

Figure 3.18: A comparison between the coherence time of the transition $5S_{1/2}(m_J = -1/2) \leftrightarrow 4D_{5/2}(m_J = -5/2)$ for both the Ramsey experiment (blue) and the Rabi oscillations (red).

Chapter 4

Summary and outlook

4.1 Summary

A stable frequency of the 674 nm qubit laser is essential in order to obtain long coherence times. Longer coherence times will allow high fidelity qubit operations on $^{88}Sr^{+}$. The frequency stability of the 674 nm laser was achieved using the PDH technique to lock the laser frequency on a high finesse cavity. The finesse of the cavity was measured to be $\mathcal{F} = (40,000 \pm 1000)$ which was significantly lower than the finesse of $> 200,000$ specified by the company. The cavity linewidth was measured to be $\Delta\nu_c = (30,700 \pm 800)$ Hz, the zero-expansion-point, the free spectral range and the frequency drifts of the cavity were also measured. By using a beat note between the 674 laser II and the 674 laser I the upper bound of the linewidth of the laser was measured to be (123 ± 6) Hz, which is likely broader than the actual linewidth since the light from the old laser travels through a 10 m fiber from the other lab and fiber noise is typically on this order of magnitude.

A Ramsey experiment on the ion was performed using the new stabilised laser setup, as well as Rabi oscillations with both the 674 laser II and the 674 laser I. The coherence time without line trigger measured in the Ramsey experiment and the coherence time measured with the Rabi oscillations are very different from one another. The Ramsey experiment gives a coherence time of $\tau = (72 \pm 3)$ μs compared to $\tau = (1050 \pm 90)\mu$s for the Rabi oscillations, suggesting that there is something wrong in the setup of the Ramsey experiment. This needs to be understood. So far the initial investigations of possible causes including problems with the AOMs and the 674 nm laser beams have not revealed the answer. Further investigating the cause of the error lies beyond the scope of this thesis.

4.2 Outlook

The cavity finesse was much lower than specified by the company. Therefore the cavity will be sent back to the company for cleaning to increase the reflectivity of the mirrors. Cavity I is in a temperature and vibration controlled box, so in order to stabilise the temperature and reduce the vibrations of cavity II it could be put in a box similar to the one used for cavity I. The 674 laser II and cavity is part of a new ion trap setup, when writing this thesis the ion trap is yet to be designed. But as shown in this thesis, it can also be used for measurements using the existing trap setup. As shown in this thesis the contrast decay of the Rabi oscillations of the 674 laser II is slightly longer than for the 674 laser I which open up new measurement possibilities on the ion. The 674 laser II with its intra-cavity EOM enables reduction of servo bumps, for some experiments the servo bumps of 674 laser I has been a limiting factor, so possible future experiments using the 674 laser II will improve these measurements and the ability to manipulate and control the ion.

Bibliography

[1] J. I. Cirac and P. Zoller, "Quantum computations with cold trapped ions," *Physical review letters*, vol. 74, no. 20, p. 4091, 1995.

[2] D. P. DiVincenzo, "The physical implementation of quantum computation," *Fortschritte der Physik: Progress of Physics*, vol. 48, no. 9-11, pp. 771–783, 2000.

[3] M. Müller, L. Liang, I. Lesanovsky, and P. Zoller, "Trapped Rydberg ions: from spin chains to fast quantum gates," *New Journal of Physics*, vol. 10, no. 9, p. 093009, 2008.

[4] G. Higgins, *A single trapped Rydberg ion*. PhD thesis, Department of Physics, Stockholm University, 2018.

[5] M. Fox, *Quantum Optics: An Introduction*. Oxford Master Series in Physics, OUP Oxford, 2006.

[6] F. Pokorny, *Experimental setup for trapping strontium Rydberg ions*. Master's thesis, University of Innsbruck, 2014.

[7] N. Röck, *Quantum manipulation on the Barium quadrupolar transition*. Master's thesis, University of Innsbruck, 2011.

[8] A. Lindberg, *Improving the coherent quantum control of trapped ion qubits*. Master's thesis, Stockholm University, 2020.

[9] F. L. Pedrotti, L. M. Pedrotti, and L. S. Pedrotti, *Introduction to optics*. Pearson Education Limited, 2014.

[10] F. Kress, *Frequenzstabilisierung eines 674 nm Diodenlasers zur Detektion der Rydberganregung von Strontiumionen*. Master's thesis, University of Innsbruck, 2015.

[11] E. D. Black, "An introduction to Pound–Drever–Hall laser frequency stabilization," *American journal of physics*, vol. 69, no. 1, pp. 79–87, 2001.

[12] M. Johnson, *PID Control Technology*, pp. 1–46. London: Springer London, 2005.

Appendices

A Settting up temperature control system for the cavity

The cavity was connected to a Peltier element and two temperature sensors (NTC thermistors) inside the vacuum chamber, these were connected to a temperature controller (SRS PTC10) using a foil-shielded twisted pair cable to reduce noise and cross-talk between the cables. The Peltier element was connected to a TEC driver card in the temperature controller using a pin connector (See figure A.1). One of the temperature sensors (NTC 1) was connected to a PTC 320 card in the temperature controller using another type of connector (See figure A.2). While the other sensor is not connected to anything permanently at the moment, but can be used for an out-of-loop temperature readout. A schematic of the cavity connector is shown in figure A.3.

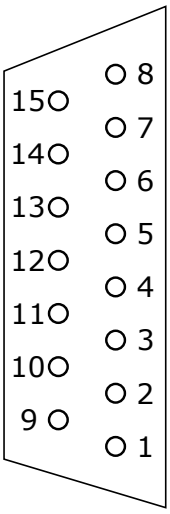

Figure A.1: A schematic of the connector used to connect the Peltier element to the TEC card. Where pin 1 and pin 2 is connected to pin 2 of the cavity connector, pin 3 and pin 4 is connected to pin 5 of the cavity connector and pin 5 is connected to the shielding. The rest of the pins are unconnected.

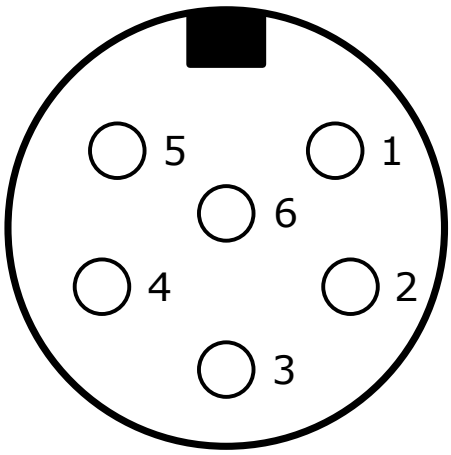

Figure A.2: A schematic of the connector used to NTC 1 to the PTC320 card. Where pin 1 and pin 2 is connected to pin 3 of the cavity connector, pin 3 is unconnected and pin 4 and pin 5 is connected to pin 1 of the cavity connector.

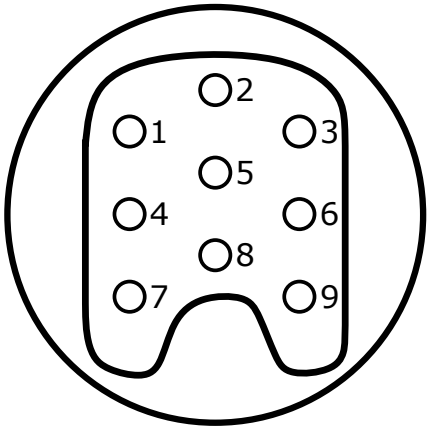

Figure A.3: A schematic of the connector used to connected to the cavity. Where pin 2 and pin 5 is connected the Peltier element, pin 1 and pin 3 is connected to NTC 1 and pin 4 and pin 6 is connected to NTC 2.

Acknowledgements

This thesis was made possible with the guidance of a few people. I would like to thank my supervisor Markus Hennrich, my assistant supervisor Gerard Higgins and PhD students Fabian Pokorny and Chi Zhang for their help and encouragements. I would also like to thank the rest of the trapped ion group at Stockholm University, PhD students Harry Parke and Shalina Salim and master student Anders Lindberg for their support. I truly enjoyed being part of this group and working with you all.